Shallow-etched thin-film lithium niobate waveguides for highly-efficient second-harmonic generation

JIE ZHAO[1,*], MICHAEL RÜSING[2], USMAN A. JAVID[3], JINGWEI LING[4], MINGXIAO LI[4], QIANG LIN[3,4] AND SHAYAN MOOKHERJEA[1]

[1] *University of California, San Diego, Department of Electrical and Computer Engineering, La Jolla, California 92093-0407, USA*
[2] *TU Dresden, Institut für Angewandte Physik, 01187 Dresden, Germany*
[3] *Institute of Optics, University of Rochester, Rochester, NY 14627, USA*
[4] *Department of Electrical and Computer Engineering, University of Rochester, Rochester, NY 14627, USA*
[*] *jiz378@eng.ucsd.edu*

Abstract: High-fidelity periodic poling over long lengths is required for robust, quasi-phase-matched second-harmonic generation using the fundamental, quasi-TE polarized waveguide modes in a thin-film lithium niobate (TFLN) waveguide. Here, a shallow-etched ridge waveguide is fabricated in x-cut magnesium oxide doped TFLN and is poled accurately over 5 mm. The high fidelity of the poling is demonstrated over long lengths using a non-destructive technique of confocal scanning second-harmonic microscopy. We report a second-harmonic conversion efficiency of up to 939 %.W^{-1} (length-normalized conversion efficiency 3757 %.W^{-1}.cm^{-2}), measured at telecommunications wavelengths. The device demonstrates a narrow spectral linewidth (1 nm) and can be tuned precisely with a tuning characteristic of 0.1 nm/°C, over at least 40 °C without measurable loss of efficiency.

1. Introduction

Efficient quasi-phase matched (QPM) three-wave mixing is important in optical parametric oscillation [1–3], wavelength conversion [4, 5] and in quantum optics [6–8]. Lithium niobate is widely used because of its wide transparent window (350 nm - 4.5 μm) and large second-order nonlinear coefficient (d_{33} = 25 pm/V). QPM can be realized in lithium niobate by periodic poling. During the poling process, the orientation of the spontaneous polarization (P_s) and the sign of d_{33} of LN is periodically reversed, which introduces a quasi-momentum that compensates the phase mismatch among the interacting waves.

Over the past few years, many efficient wavelength converters have been demonstrated based on x-cut and y-cut thin-film PPLN waveguides [9–14]. Because of the tight light confinement in the thin-film waveguides, more than one order of magnitude improvement have been achieved in the normalized conversion efficiency (η_{norm}) [11], compared to the traditional proton-exchanged bulk LN waveguides [15]. A brief summary of the existing works is presented in Table 1 in the Appendix. This waveguide structure allows access to the highest second-order nonlinear coefficient of LN (d_{33}), and enables poling with electrodes fabricated on the surface of the thin film of LN. The required poling period (Λ) for the first-order QPM in TFLN waveguides is generally much smaller than that of the bulk waveguides, because of the high dispersion of the confined modes with smaller cross-sectional area. As is shown in Table 1, in most of the reported TFLN SHG devices, Λ is 4 - 6 μm. The theoretical η_{norm} can be further improved, according to our simulations as well as the simulations in Refs. [12, 14], if a lower value of Λ can be fabricated. However, lateral spreading of the inverted domains becomes non-negligible when Λ gets smaller, which hinders the realization of $\sim$ 50% poling duty cycle and more importantly,

adjacent domains may merge before the thin film is completely inverted in depth. Recently, Rao *et al.* [14] have demonstrated a high value of $\eta_{\text{norm}} \approx 4600$ %.W^{-1}.cm^{-2} from a relatively short etched PPLN waveguide (0.3 mm length). However, because the length of the waveguide is on sub-millimeter scale, the measured conversion efficiency (η) is still significantly lower than other bulk or thin-film devices (see Table 1). Therefore, as is mentioned by the authors, the uniformity of poling needs to be further improved, to achieve a comparable conversion efficiency (η) as in the bulk PPLN waveguides. While the conversion efficiency can be further enhanced through resonant structures, as have been demonstrated in z-cut TFLN microrings very recently [16], the operating temperature range is limited, and the device performance is more sensitive to the fabrication errors. Thus, it is important to understand and improve the poling process for longer waveguides, and at the same time, design waveguide structures whose SHG performance will remain relatively insensitive to fabrication or layer-thickness variations as the device length is increased.

Periodic poling of x-cut TFLN is realized by the application of a strong electric field to the crystal through lithographically-defined surface electrodes. The poling voltage is significantly lower than in traditional LN devices, since the electrode gap separation is on the order of a few tens of microns, rather than hundreds of microns or millimeters. For x-cut TFLN, we require that the poled domains are completely inverted in depth (i.e., along the x axis). Conventional techniques of evaluating poling quality are selective hydrofluoric acid (HF) etching, piezo-response force microscopy (PFM), and Raman microscopy. Selective HF etching is destructive and is especially difficult to control for TFLN chips which include silicon dioxide in the layer stack. PFM is best suited for investigating surface structures, and does not yield complete information about the poling quality over the depth of the waveguide mode, which is a few hundreds of nanometers in thickness. In bulk crystals, confocal Raman microscopy [17–19] can provide a 3D visualization of domains, but offers a depth resolution only of about 1 μm, which is too large for the TFLN thickness. Therefore, these methods are unsuitable for obtaining detailed information about the poled structures under study here. Instead, we use confocal scanning second-harmonic microscopy, which can image the inverted domains in both bulk and thin-film LN non-invasively [20–26]. This technique allows us to unambiguously distinguish between a fully-inverted and partially-inverted film in depth within the limits of lateral resolution [27, 28]. Here, we use this technique to understand and optimize our poling recipe, and thus, we were able to demonstrate (as shown by super-resolution microscope images, reported below) uniformly-inverted domains over a 5 mm long poling region, with a 2.8 μm period. This ability to non-destructively identify and use well-poled TFLN regions in which to fabricate the best-performing waveguides is expected to be broadly useful for improving the yield of high-performance TFLN waveguides.

Through design, we also address the sensitivity of the SHG conversion process to variations in waveguide width over these longer lengths. In general, TFLN waveguides are formed by physically structuring (e.g., etching or dicing) LN, or by rib-loading the LN film with a second material, e.g., silicon nitride. The etched TFLN waveguides can provide a higher degree of mode confinement and higher conversion efficiency than the hybrid waveguides. However, a long-standing and unresolved concern, as is mentioned recently by Boes *et al.* [13], is that the QPM wavelength (λ_{p}) is highly sensitive to the waveguide dimensions, e.g., width (w), which is exacerbated in TFLN structures, compared to bulk LN devices. Here, we use a waveguide design for improving the tolerance to fabrication non-uniformities, achieving similar width-sensitivity as that of the rib-loaded (unetched LN) waveguide structure, but also has the higher conversion efficiency as that of the etched waveguide. This is achieved using a shallow-etched waveguide structure [see Figs. 1(a)-(b)] in which the x-cut TFLN film thickness is 300 nm and the etching depth is 50 nm. From measurements reported below, we measured SHG with η_{norm} and η are 3757 %.W^{-1}.cm^{-2} and 939 %.W^{-1} respectively, and a relatively-low width sensitivity of $(d\lambda_{\text{p}}).(dw)^{-1} = -0.064$. This number is similar to what is recently reported for a hybrid

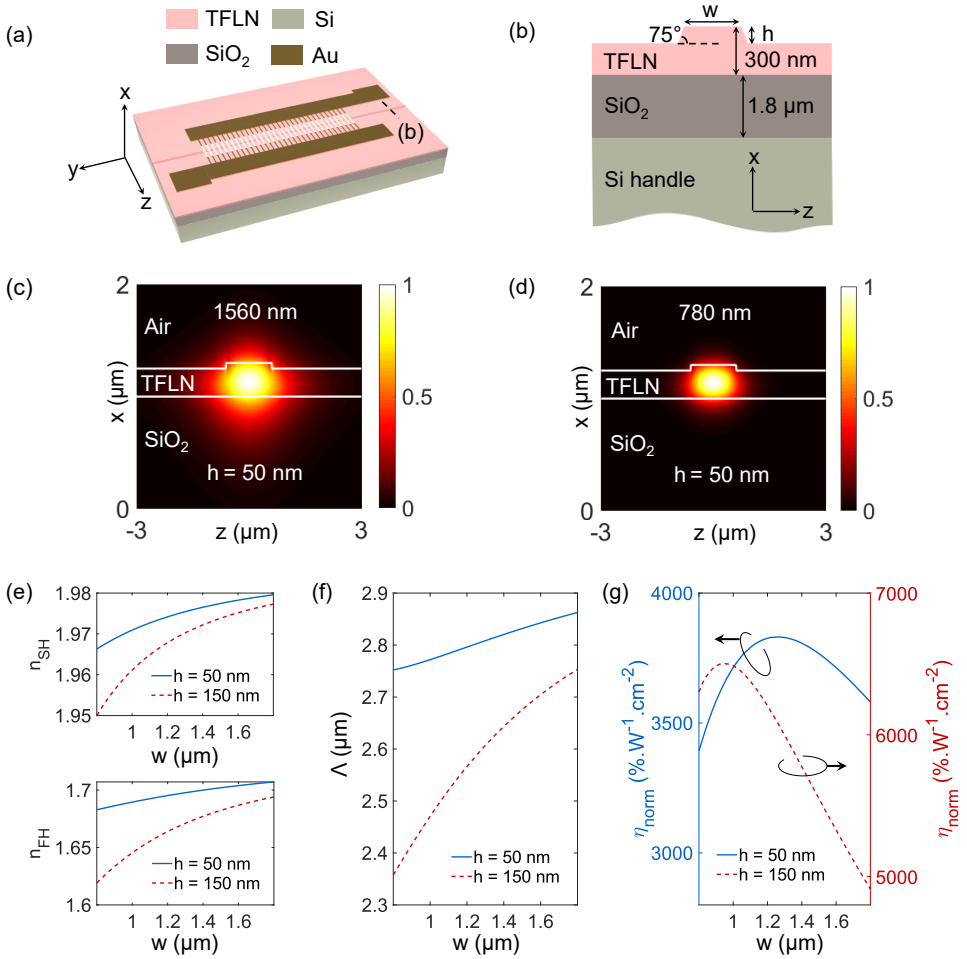

Fig. 1. (a)-(b) Schematic illustration of the PPLN waveguide with poling electrodes (a), and the waveguide cross-section (b). (c)-(d) Simulated mode profiles (intensity of the electric field) of the fundamental TE mode at 1560 nm (c) and 780 nm (d). The x-cut TFLN layer has a crystal axis oriented along the z axis, and the waveguide extends along the y axis. (e)-(g) Simulated mode indices ($n_{\{\mathrm{SH,FH}\}}$ represents the mode index at the SH and pump wavelengths), poling periods and normalized nonlinear conversion efficiency versus waveguide width for h = 50 nm and h = 150 nm respectively.

SiN-TFLN waveguide [13], whose conversion efficiency is one-third that of the waveguide reported here. In addition, same measurements were performed on the waveguide over a time period of more than six months, as well as at different temperatures, which proves that the high performance can be maintained over time and also through a temperature range of 40 °C.

2. Design

Quasi-analytical arguments that support the use of shallow-etched waveguides for improved tolerance to variations in the waveguide dimensions, and also relaxing the constraints on the required poling period, can be explained in terms of a simplified theory of SHG which assumes that pump depletion and loss are negligible. Specifically, we consider SHG from 1560 nm to 780 nm, using the quasi-TE-polarized fundamental modes in a waveguide whose cross section

is shown in Fig. 1(b), where the TFLN thickness is 300 nm. Under the stated approximations, the power of the generated second-harmonic wave P_{SH} from the pump P_{FH} can be calculated using Eq. 3 (Appendix, assuming zero propagation loss). The normalized nonlinear conversion efficiency is defined as:

$$\eta_{\mathrm{norm}} = \frac{P_{\mathrm{SH}}}{P_{\mathrm{FH}}^2 L_{\mathrm{NL}}^2} \times 100\%, \tag{1}$$

where L_{NL} is the length of the nonlinear interaction region, which is also the length of the poled region.

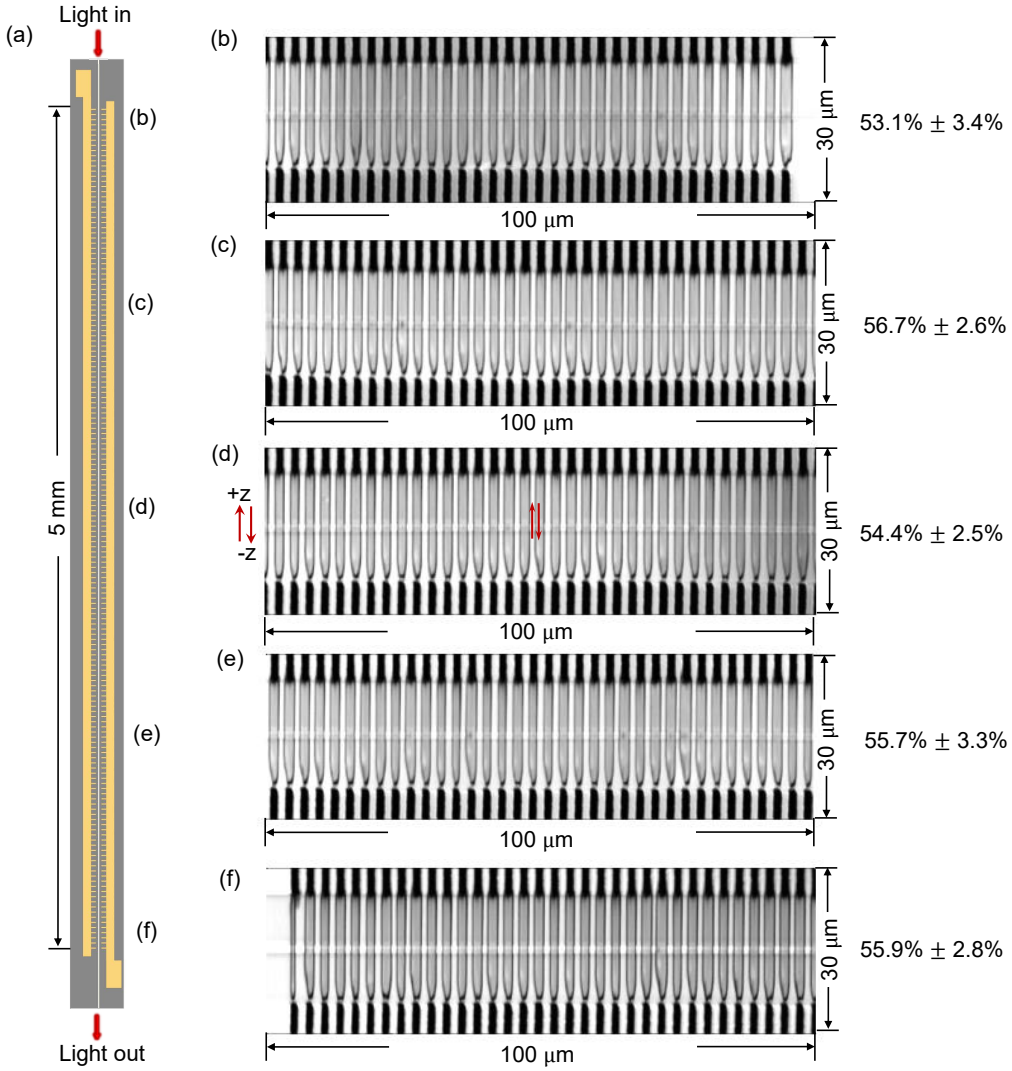

Fig. 2. (a) Schematic of the waveguide with poling electrodes. (b)-(f) Second-harmonic images of the inverted domains at the locations indicated in (a), with the calculated poling duty cycles listed on the side. The light gray left-to-right stripe visible in each of the panels is the ridge structure of the waveguide that is formed by shallow etching [see Fig. 1(b)]. The image of each panel is rotated clockwise by 90 degrees from the orientation of panel (a).

To calculate η_{norm}, Lumerical MODE Solutions was used to simulate the modes at the pump

and SH wavelengths. In the simulation, we used d_{33} = 25 pm/V, which is the same as reported in the previous publications [11]. As an example, the calculated mode profiles of the fundamental TE mode at 1560 nm and 780 nm are shown in Figs. 1(c)-(d), for w = 1.2 μm and h = 50 nm. In terms of fabrication process tolerance, Figs. 1(e)-(f) show that shallow-etched waveguides (h = 50 nm) are less sensitive to waveguide width variations. Furthermore, shallow-etched waveguides may incur less propagation loss due to edge roughness. As Fig. 1(f) shows, we can use a larger poling period for shallow-etched structures, which leads to easier fabrication and a better fidelity to design. Both types of waveguides have an optimal width; Fig. 1(g) shows that the nonlinear conversion efficiency for the shallow-etched waveguide is maximized when w = 1.2 μm, with the effective mode areas being 1.1 μm^2 at 1560 nm and 0.4 μm^2 at 780 nm. Such waveguide structures provide for a good overlap between the quasi-TE-polarized fundamental modes at the widely-separated pump [Fig. 1(c)] and the SH [Fig. 1(d)] wavelengths, calculated to be O =78% based on the standard equation below:

$$O \equiv |\mathrm{Re}[\frac{(\int \vec{E}_1 \times \vec{H}_2^* \cdot \mathrm{d}\vec{S})(\int \vec{E}_2 \times \vec{H}_1^* \cdot \mathrm{d}\vec{S})}{\int \vec{E}_1 \times \vec{H}_1^* \cdot \mathrm{d}\vec{S}}] \times \frac{1}{\mathrm{Re}(\int \vec{E}_2 \times \vec{H}_2^* \cdot \mathrm{d}\vec{S})}|, \tag{2}$$

where $\vec{E}_{\{1,\,2\}}$ and $\vec{H}_{\{1,\,2\}}$ represents the electric and magnetic fields at the pump and SH wavelength respectively. Based on these considerations, our optimum waveguide width was 1.2 μm, etching depth was 50 nm, and poling period was 2.8 μm.

3. Device fabrication

An x-cut LNOI wafer (5 mol% MgO doped) with 300 nm LN thickness was obtained from a commercial source (NanoLN, Jinan Jingzheng Electronics Co., Ltd.). Poling electrodes with a uniform 2.8 μm period were first defined on the x-cut LNOI surface using the standard photolithography process. In cross-section, the electrodes consist of a 10 nm Cr adhesion layer deposited on TFLN, followed by a 300 nm Au layer. The separation gap between the two opposing electrode "teeth" facing each other was designed to be 20 μm, based on an estimate of the critical field required to initiate poling. The device was poled in transformer oil to prevent electrode breakdown. A single high voltage pulse (around 800 V) was applied to the poling circuit through a high-voltage amplifier, using a voltage waveform described in Ref. [27]. Next, the waveguides were formed in the middle of the poled region using electron-beam lithography and argon ion milling for etching. We did not remove the poling electrodes. Multiple waveguides were fabricated on this chip, with varying waveguide widths. (The actual etching depth was ~48 nm, and the resist shrinkage was estimated to be about 100 nm. These values will be taken into account in the theoretical calculations discussed below.) The waveguide propagation losses at the pump and SH wavelengths are less than 1 dB/cm and 3.2 dB/cm respectively, estimated by measuring the insertion loss of waveguides with different lengths (the cutback method), performed on five waveguides for each length. In this study, we did not observe a clear correlation between the total insertion loss and waveguide width. The length of the etched waveguide is 7 mm, without tapered edge-couplers, while the poled region is 5 mm, as is illustrated in Fig. 2(a). Second-harmonic microscopy is used here to image the inverted domains. Typical domain structures are shown in Figs. 2(b)-(f), in which the dark stripes at the top and bottom of the images are the poling electrodes, the bright rectangle in the middle of the images represents the etched waveguide, and the black straight lines that start from the top (positive) electrodes and terminate at the bottom (ground) electrodes are the domain walls. In between the opposing poling electrodes, the orientation of P_s is reversed, which is indicated by the red arrows in Fig. 2(d). The inverted and uninverted regions are separated by the domain walls. Details of the SH measurement technique and analysis are reported elsewhere [27, 28]. To calculate the poling duty cycle, five SH images were generated over several segments along the waveguide, each

with an area of 100 μm $\times$ 30 μm, as is shown in Figs. 2(b)-(f). For this test chip, the poling duty cycle varied from 45% to 60%. For the three waveguides reported in the manuscript, the waveguide widths were 1.14 μm, 1.24 μm and 1.32 μm respectively. Based on the SH images, the poling duty cycles mean value and one standard deviation were: 57.2% ± 3.5%, 55.2% ± 3.0% and 46.4% ± 4.4%, respectively. The quantification method is described in the Appendix. As demonstrated by detailed simulations in Ref. [28], for domains completely inverted in depth, the detected SH signal should be the same from poled and unpoled regions. Here, we observe similar SH signal levels in the inverted and unpoled regions nearby [see Figs. 2(b)-(f)], which indicates domains inverted toward almost the complete film thickness.

4. Second harmonic generation

A continuous-wave telecom-wavelength tunable laser (ANDO AQ4320D) was used as the pump source along with a polarization controller to ensure that the pump light was TE-polarized. Light was coupled in and out of the chip with polarization-maintaining tapered lensed fibers. A 780 nm power sensor together with a power meter was connected to the output tapered lensed fiber to detect and record the generated SH power. The chip was mounted on a temperature-controlled stage with a thermo-electric controller (TEC) in feedback with a thermistor on the stage mount. The generated off-chip SH power was measured and recorded by a power meter, and the on-chip SH power was calculated using the recorded off-chip power divided by the coupling efficiency. The conversion efficiency was then calculated using Eq. 1.

To study the stability of these waveguides as well as the repeatability of the measurements, we measured SHG from this chip over a time period of more than six months. In the initial experiments, the chip was simply diced for measurement, without edge polishing, and thus incurred somewhat high, un-optimized coupling losses to standard, telecom-wavelength, lensed tapered fibers (no index-matching fluid) of 7.7 dB/facet at 1560 nm, and 13.9 dB/facet at 780 nm, calculated based on the measurements from a ~1.32 μm wide waveguide. In addition to the edge roughness, the high coupling loss at the SH wavelength is dominated by the mode mismatch between the focused fiber mode (mode field diameter: 2.5 μm) and the waveguide mode (effective mode area: ~0.4 μm^2), as well as the propagation loss in the telecom-wavelength fibers. This issue is not uncommon for TFLN waveguides, and can be addressed by edge polishing, adding tapers and edge couplers, and using 780 nm fibers for output coupling [9, 10, 29]. Figure 3(a) shows the measured nonlinear conversion efficiency as a function of the pump wavelength for this waveguide at 20 °C. Note that each SHG spectrum shown below is an averaged result of several measurements. The extracted on-chip normalized conversion efficiency has a peak value of 2658 %.W^{-1}.cm^{-2} at 1553.6 nm. Figure 3(b) shows the measured on-chip pump power versus the generated SH power, where the power conversion efficiency reaches 9.4% with the on-chip pump power being 16.7 mW. The black solid line follows $\eta_{\text{norm}} L_{\text{NL}}^2 P_{\text{pump}}^2$, with η_{norm} being 2658 %.W^{-1}.cm^{-2}, while the red dashed line plots the calculated input pump and output SH power based on the coupled mode equations. Based on Fig. 3(b), we see evidence of sub-quadratic scaling at an (on-chip) launched pump power of about 10 mW. At higher pump power, the measured SH power is lower than the quadratic curve, which suggests the onset of pump depletion. We performed the SHG measurements on this chip again after chip edge polishing. Figure 3(c) shows measured SHG spectrum from a 1.14 μm wide waveguide, with a peak η_{norm} of 3757 ± 39 %.W^{-1}.cm^{-2} (peak η = 939 ± 10 %.W^{-1}). The uncertainty here arises from the fluctuations in the optical power levels from multiple measurements. After edge polishing, the coupling loss was 6.7 dB/facet at 1560 nm, and 12.5 dB/facet at 780 nm. The oscillations in the SHG spectrum are from the Fabry-Perot resonances at both the pump and SH wavelengths, caused by the reflections at the polished waveguide facets. Based on our FDTD simulation, the reflectivity at the pump and SH wavelength is 12.7% and 16.8% respectively, for perfectly smooth waveguide facets. For a lightly polished (with a non-zero roughness) facet

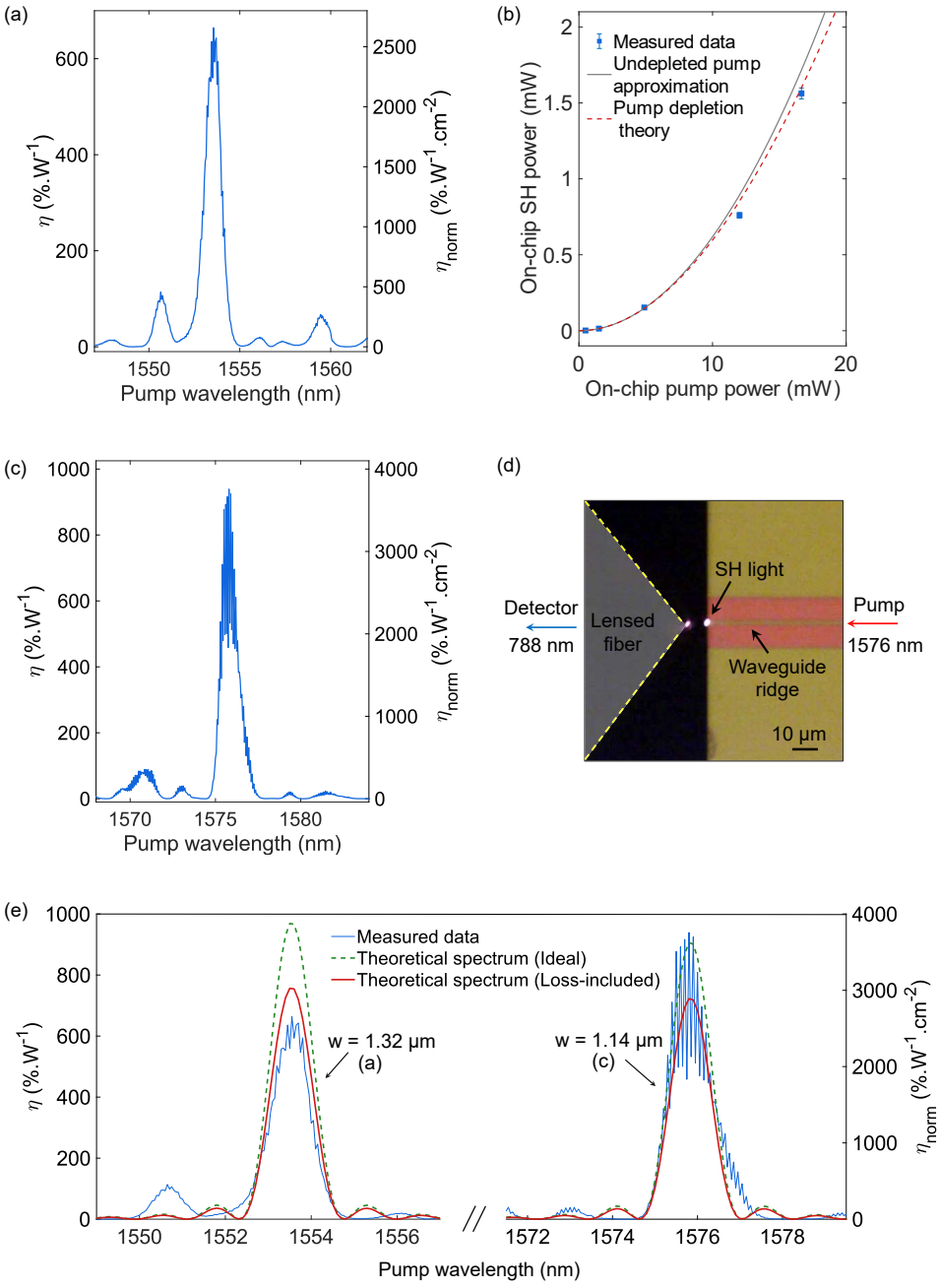

Fig. 3. (a) Measured η (left y-axis) and η_{norm} (right y-axis) as a function of the pump wavelength, for a 1.32 μm wide waveguide. (b) Measured on-chip pump power versus on-chip SH power at the peak pump wavelength. Errorbars represent one standard deviation in the calculated on-chip SH power from multiple measurements. The solid black line follows $\eta_{\text{norm}} L_{\text{NL}}^2 P_{\text{pump}}^2$ ($\eta_{\text{norm}} = 2658$ %.W^{-1}.cm^{-2}). The dashed red line plots the calculated on-chip pump and SH power based on the coupled-mode equations. (c) Measured η (left y-axis) and η_{norm} (right y-axis) as a function of the pump wavelength for a 1.14 μm wide waveguide, after chip edge polishing. (d) Image captured by a CCD camera at the output waveguide facet, showing the scattered SH light, waveguide and the lensed fiber. The on-chip SH power was 2.66 μW (measured power: 150 nW) at 788 nm, with ~0.53 mW on-chip pump power at 1576 nm. (e) Comparison of the theoretical SHG tuning curve with measured spectrum for the 1.32 μm and 1.14 μm wide waveguides.

fabricated here, the reflectivity should be lower than the theoretical value [30]. Figure 3(d) is an image captured by a CCD camera at the output waveguide facet of the 1.14 μm wide waveguide, while the waveguide was pumped with about 0.53 mW power at 1576 nm. The generated on-chip SH power, as is indicated in Fig. 3(d) was 2.66 μW (measured power: 150 nW). Comparison of the measured SHG spectrum before and after edge polishing is shown in section A4 in the Appendix.

Using the simulated mode indices and profiles from Lumerical MODE Solutions, the theoretical SHG spectrum can be calculated. Details of the calculation is presented in section A3 in the Appendix. The theoretical SHG spectra for these two waveguides are plotted in Fig. 3(e), overlaid with the measured curves. By assuming $\Lambda = 2.81$ μm (compared to the design target of 2.80 μm), the simulated peak wavelength accurately matches the measured value of the peak wavelength, as shown in Fig. 3(e). The green dashed lines represent the ideal SHG spectra from a lossless waveguide, while the red solid lines plot the corrected spectra considering the measured waveguide propagation losses at both the pump and SH wavelengths. For the 1.32 μm wide waveguide, the measured peak efficiency is slightly lower than the theoretical value, which is probably due to the undesired sidelobe at around 1550.7 nm. Poling period (i.e., period of the poling electrodes) and film thickness variations, as well as the un-optimized pump light polarization can result in such sidelobes as seen here. Previously, this has been studied for bulk PPLN [31–33], and comparable inferences can be made for TFLN as well. For example, the calculated poling period for the highest side peak in Fig. 3(a) at 1550.7 nm is 2.805 μm, while that for the central lobe at 1553.6 nm is 2.808 μm, i.e., a shift of only 3 nm. The measured SHG spectrum of the 1.14 μm wide waveguide shows an otherwise higher peak efficiency than the predicted value, which can be partly attributed to the enhanced pump power in the cavity by the Fabry-Perot resonances, as has been discussed in Ref. [13]. Nevertheless, the full-width at half-maximum (FWHM) spectral bandwidth of the measured spectra are 1.04 nm and 1.01 nm for the two waveguides, which is almost the same as the theoretical value. This good agreement proves the excellent uniformity of the periodically poled waveguide over the entire poling region.

5. Tolerance and tuning of the spectrum

To evaluate the tolerance of this shallow-etched waveguide to fabrication errors, we measured the SHG spectra from different waveguides with the width varying from 1060 nm to 1340 nm. Figure 4(a) shows the simulated poling period (Λ) versus pump wavelength for waveguides with different widths. In the fabricated device, Λ is fixed at 2.8 μm, which is indicated as a black dashed line in Fig. 4(a). Wider waveguides are phase matched at shorter wavelengths. Taking the intersections of the dashed line with the curves shown in Fig. 4(a), we obtained the simulated λ_p as a function of waveguide width, which is shown in Fig. 4(b) as blue squares. On the other hand, from the recorded SHG spectra, we can acquire the measured λ_p, which are plotted as the red circles in Fig. 4(b). The fitted tuning slope from the measured $[(d\lambda_p).(dw)^{-1} = -0.064]$ and simulated $[(d\lambda_p).(dw)^{-1} = -0.088]$ data agrees well with each other. The measured tuning slope is only -0.064, which is similar to the silicon nitride loaded, unetched TFLN waveguides [13]. This suggests that the shallow-etched waveguides fabricated here manage to have a very high tolerance to fabrication errors that is comparable to the unetched hybrid SiN-TFLN waveguides, and at the same time achieve a higher nonlinear conversion efficiency, taking the advantage of better mode confinement in the etched structures. For this study, the etching depth (h), or the waveguide ridge height is fixed at 50 nm. But we have simulated the peak wavelength shift versus etching depth variation for a 1.2 μm wide waveguide. As is shown in Fig. 4(c), the simulated $(d\lambda_p).(dh)^{-1}$ is 2.59.

We have also studied the thermal tuning characteristic of the shallow-etched waveguide by varying the TEC temperature from 20 °C to 60 °C and recorded the SHG spectra, which are plotted in Fig. 4(c). As is shown in Fig. 4(d), the measured λ_p scales almost linearly with the

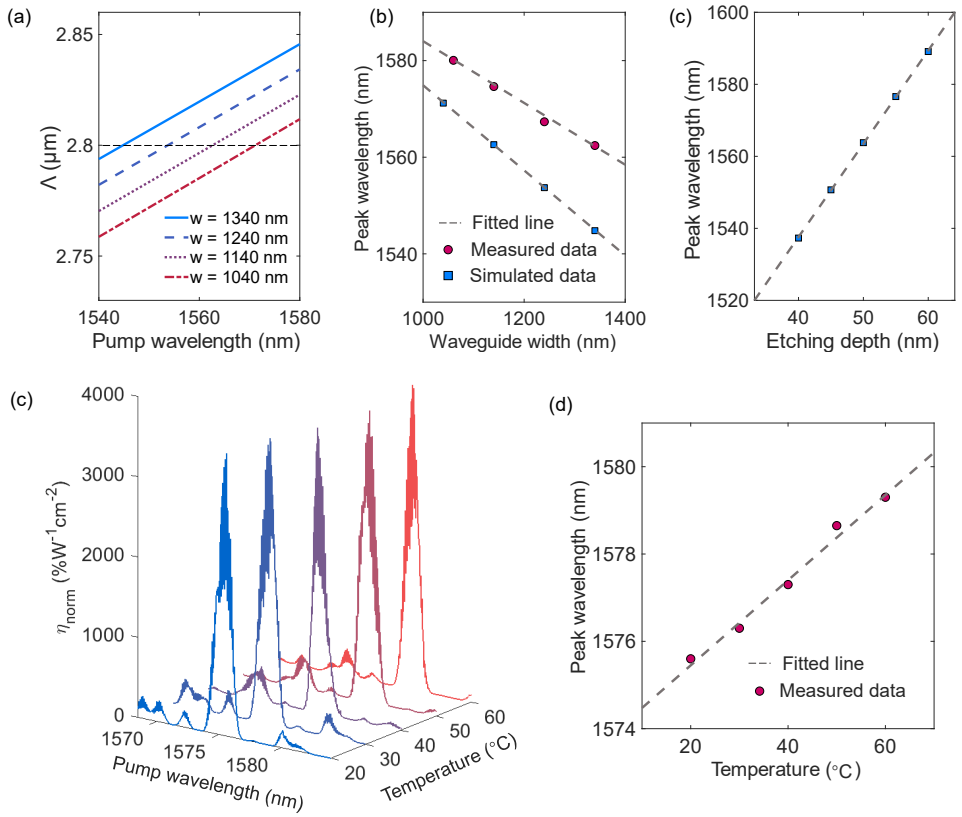

Fig. 4. (a) Simulated poling period (Λ) as a function of pump wavelength for waveguides with different widths. (b) Measured (red circles) and simulated (blue squares) peak pump wavelength (phase-matched pump wavelength λ_p) versus the waveguide width. (c) Simulated peak pump wavelength (phase-matched pump wavelength λ_p) versus the etching depth. (d)-(e) Measured SHG spectra (d) and λ_p (e) with different TEC temperatures.

TEC temperature, and the fitted $(d\lambda_p).(dT)^{-1}$ is about 0.1 nm/°C, which is similar to that of the bulk LN waveguides [32, 34]. The simulated $(d\lambda_p).(dT)^{-1}$ (not shown here) is 0.43 nm/°C, taking into account the temperature and wavelength dependence of the material indices of LN and SiO_2 [35–37]. This discrepancy may come from the differences in the actual temperature-dependent material properties compared to the assumptions made in the simulation. Same measurements have been performed on this waveguide before edge polishing, more than six months apart, which presented the same tuning slope as shown in Fig. 4(d).

6. Conclusion

In summary, we design and demonstrate a shallow-etched thin-film MgO:PPLN waveguide structure that achieves the highest (non-length-normalized) conversion efficiency for SHG from telecommunications wavelengths between 1550 nm and 1580 nm to the near-infrared wavelength range of wavelengths between 775 nm and 790 nm. The main achievement is the improvement (see Table 1) in non-length-normalized conversion efficiency of periodically-poled TFLN waveguides, which may be considered more promising for making the case for practical and realistic device applications of TFLN than high values of only the length-normalized figure of merit. Using confocal scanning second-harmonic microscopy as a non-invasive diagnostic

method, we demonstrate successful fabrication of uniformly-inverted domains with a 2.8 μm period and nearly ideal duty cycle over a 5 mm long region. The efficient and narrow linewidth SHG spectrum can be useful for direct conversion of telecommunications-band signals, which are typically on a 100 GHz (0.8 nm) grid. The thermal-tuning characteristics demonstrated a linear tuning sensitivity of $(d\lambda_p).(dT)^{-1}$ is 0.1 nm/°C, and showed that efficiency was maintained over a temperature swing of up to 40 °C. The shallow-etched waveguide possesses a high tolerance to fabrication errors in width, with a measured $(d\lambda_p).(dw)^{-1}$ being -0.064, which is comparable to what was reported from an unetched hybrid SiN-TFLN waveguide. The results demonstrated here indicate promising applications for robust and efficient waveguide TFLN devices for applications in nonlinear optics in the telecommunications regime.

7. Appendix

7.1. Summary of the existing works

Table 1. Existing works of thin-film PPLN based SHG devices, in comparison with the most efficient bulk PPLN waveguide. N/A: cannot be inferred from the reported data.

Ref.	Type	η (%.W^{-1})	η_{norm} (%.W^{-1}.cm^{-2})	FWHM (nm)	Λ (μm)	Length (mm)
[15]	Annealed RPE:LN	1634	150	0.26 [a]	15.5	33
[9]	SiN-TFLN	37	160	3.0	6.6	4.8
[11]	Etched TFLN	416	2600	7.1 [b]	4.1	4
[11]	Etched TFLN	368	2300	12.0 [b]	4.1	4
[12]	Etched TFLN	352	2200	3.2 [c]	4	4
[13]	SiN-TFLN	267	1160	2.1	4.98	4.8
[14]	Etched TFLN	4	4600	14.0 [d]	N/A	0.3
[14]	Etched TFLN	10	2800	9.1 [d]	2.67	0.6
This work	Shallow-etched TFLN	939	3757	1.0	2.8	5

[a] Estimated from Fig. 2 (in the paper). [b] Estimated from Fig. 3(c) and Fig. 3(b). [c] Estimated from Fig. 3(a). [d] Estimated from Fig. 2(f) and Fig. 2(c).

7.2. Poling duty cycle calculation

The poling duty cycle is defined as $\xi = w_D/\Lambda \times 100\%$, where w_D is the width of the inverted domain, and Λ is the poling period. As shown in Fig. 2 in the manuscript, the width of the inverted domains was seen to remain the same across most of the 20 μm wide gap between the electrodes, except for the region close to the ground electrode. The waveguide occupies a relatively small portion of the distance. The domain width w_D is calculated from two line-scans in the poling region separated by a distance of 6 μm, which is large enough to cover the optical mode [see Figs. 1(c)-(d)], with the waveguide sitting in the center. To calculate the poling duty cycle, five SH images were obtained along the entire 5 mm-long waveguide, each covering an

area of 100 μm × 30 μm, as is shown in Fig. 2; Fig. 5 shows one of the SH images from a 1.32 μm wide waveguide as an example. The width of each individual domain is calculated based on the two line-scans, from which we can get a distribution of the poling duty cycle for this 5 mm long waveguide. For each waveguide, the mean value and the standard deviation of ξ was calculated from an analysis of about 180 domains. As is shown in Fig. 5(b), the duty cycles calculated from

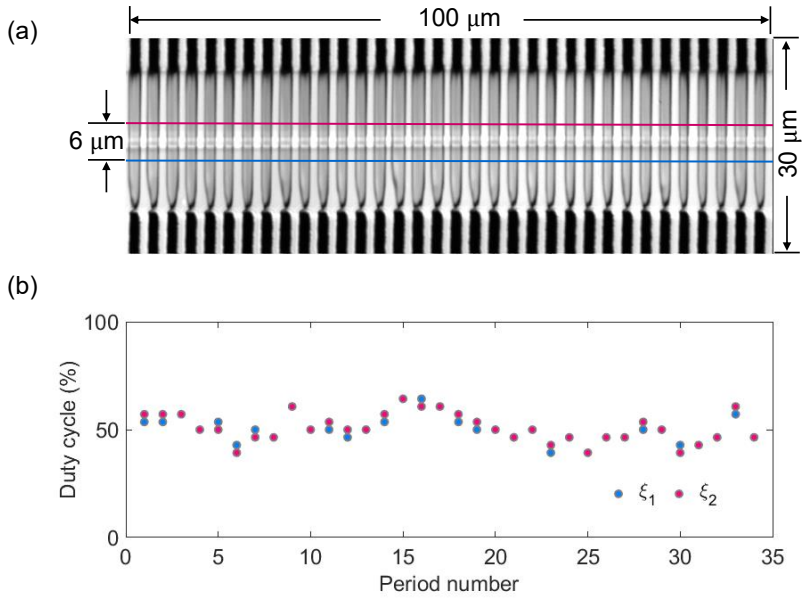

Fig. 5. (a) SH image of the inverted domains from a 1.32 μm wide waveguide. (b) Calculated duty cycles of each inverted domain based on the line-scans taken from the blue and red lines indicated in (a). The lateral spacing between the line scans is sufficient to capture the full extent of the optical mode. Other line scans within this range yield the same results.

7.3. SHG spectrum simulation

The generated SH power can be derived as [38, 39]:

$$P_{\mathrm{SH}} = \left(\frac{2}{\pi}\right)^2 \frac{8\pi^2 |\Gamma|^2 P_{\mathrm{FH}}^2 L_{\mathrm{NL}}^2}{n_{\mathrm{SH}} n_{\mathrm{FH}}^2 c \epsilon_0 \lambda_{\mathrm{FH}}^2} e^{-(\alpha_{\mathrm{FH}}+\alpha_{\mathrm{SH}}/2)L_{\mathrm{NL}}} \times \left[\frac{\sin^2\left(\frac{\Delta k L_{\mathrm{NL}}}{2}\right) + \sinh^2\left(\frac{(\alpha_{\mathrm{FH}}-\alpha_{\mathrm{SH}}/2)L_{\mathrm{NL}}}{2}\right)}{\left(\frac{\Delta k L_{\mathrm{NL}}}{2}\right)^2 + \left(\frac{(\alpha_{\mathrm{FH}}-\alpha_{\mathrm{SH}}/2)L_{\mathrm{NL}}}{2}\right)^2}\right], \tag{3}$$

where $\Delta k = k_{\mathrm{SH}} - 2k_{\mathrm{FH}} - 2\pi/\Lambda$, and Λ is the poling period of the TFLN. $\lambda_{\{\mathrm{FH,\ SH}\}}$, $n_{\{\mathrm{FH,\ SH}\}}$, $k_{\{\mathrm{FH,\ SH}\}}$, and $\alpha_{\{\mathrm{FH,\ SH}\}}$ are the wavelength, mode index, wavevector, and the waveguide propagation loss of the fundamental TE mode for the pump and SH waves, respectively, c is the speed of light in vacuum, ϵ_0 is the vacuum permittivity, and L_{NL} is the length of the nonlinear interaction region. Γ is the nonlinear mode overlap between the pump and SH waves, and is defined as:

$$\Gamma = \iint_A \boldsymbol{\varepsilon}_{\mathrm{SH}}^*(x,z)\boldsymbol{d}(x,y,z)\boldsymbol{\varepsilon}_{\mathrm{FH}}(x,z)\boldsymbol{\varepsilon}_{\mathrm{FH}}(x,z)\,dx\,dz, \tag{4}$$

where $\boldsymbol{\varepsilon}_{\{\mathrm{FH,\ SH}\}}$ is the transverse mode profile at the pump and SH wavelength respectively. $\boldsymbol{d}(x, y, z)$ is a function of d_{33}, which is only nonzero in the area where the TFLN sits:

$$\boldsymbol{d}(x, y, z) = \frac{2}{\pi} d_{\mathrm{eff}}(x, z) e^{i2\pi y/\Lambda} \hat{z},$$
$$d_{\mathrm{eff}}(x, z) = \begin{cases} d_{33}, & \mathrm{LN} \\ 0, & \mathrm{Other\ region} \end{cases} \tag{5}$$

More details can be found in Ref. [39]. Using the simulated mode indices and profiles from Lumerical MODE Solutions, the SHG spectrum can be calculated.

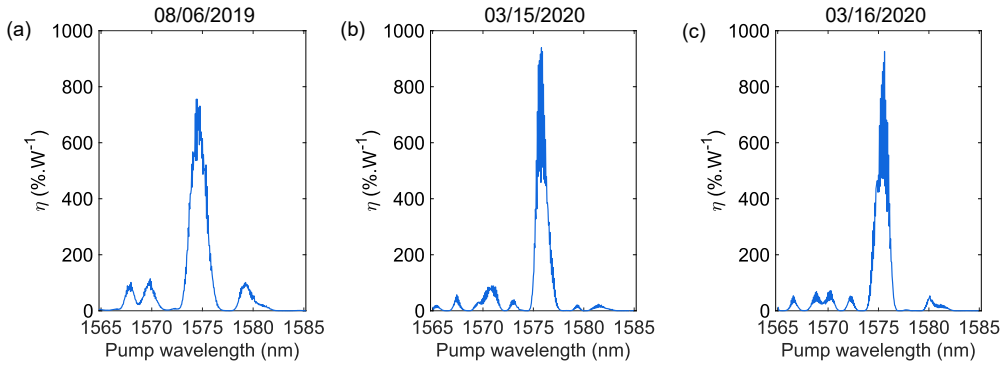

Fig. 6. Measured SHG spectra from the same waveguide on different dates.

The measured SHG spectra of the 1.14 μm wide waveguide on different dates are shown in Fig. 6, each curve is an averaged result of several measurements on the same day. The spectrum measured before edge polishing [i.e., in Fig. 6(a)] is a bit broader and with slightly higher sidelobes, which is probably due to the un-optimized polarization of the input pump light that can be altered by rough edges of the earlier chip, and thus has a slightly lower peak η compared to those measured after edge polishing. The slight shift of the phase-matched pump wavelength (1574.6 nm on 08/06/2019, 1575.8 nm on 03/15/2020, and 1575.6 nm on 03/16/2020) probably comes from the environment fluctuations (e.g., the humidity), because the waveguides were directly exposed to the air without any top cladding material. Therefore, to further improve the stability of this device, the chip can be encapsulated and packaged, as is generally performed for traditional PPLN waveguides. Nevertheless, the multiple SHG spectra presented here prove that the high performance of this device can be maintained up to at least six months.

Funding

Sandia National Laboratories (Contract Agreement 1655264); National Science Foundation (NSF) (EFMA-1640968, EFMA-1641099).

Disclosures

The authors declare that there are no conflicts of interest related to this article.

References

1. L. E. Myers, R. C. Eckardt, M. M. Fejer, R. L. Byer, W. R. Bosenberg, and J. W. Pierce, "Quasi-phase-matched optical parametric oscillators in bulk periodically poled $LiNbO_3$," J. Opt. Soc. Am. B **12**, 2102–2116 (1995).
2. S. D. Butterworth, V. Pruneri, and D. C. Hanna, "Optical parametric oscillation in periodically poled lithium niobate based on continuous-wave synchronous pumping at 1.047 microm." Opt. Lett. **21**, 1345–1347 (1996).
3. L. Lefort, K. Puech, S. D. Butterworth, G. W. Ross, P. G. Smith, D. C. Hanna, and D. H. Jundt, "Efficient, low-threshold synchronously-pumped parametric oscillation in periodically-poled lithium niobate over the 1.3 μm to 5.3 μm range," Opt. Commun. **152**, 55–58 (1998).
4. K. R. Parameswaran, J. R. Kurz, R. V. Roussev, and M. M. Fejer, "Observation of 99% pump depletion in single-pass second-harmonic generation in a periodically poled lithium niobate waveguide," Opt. Lett. **27**, 43–45 (2002).
5. R. V. Roussev, C. Langrock, J. R. Kurz, and M. M. Fejer, "Periodically poled lithium niobate waveguide sum-frequency generator for efficient single-photon detection at communication wavelengths," Opt. Lett. **29**, 1518–1520 (2004).
6. T. Inagaki, N. Matsuda, O. Tadanaga, M. Asobe, and H. Takesue, "Entanglement distribution over 300 km of fiber," Opt. Express **21**, 23241–23249 (2013).
7. N. Montaut, L. Sansoni, E. Meyer-Scott, R. Ricken, V. Quiring, H. Herrmann, and C. Silberhorn, "High-efficiency plug-and-play source of heralded single photons," Phys. Rev. Appl. **8**, 024021 (2017).
8. M. Bock, A. Lenhard, C. Chunnilall, and C. Becher, "Highly efficient heralded single-photon source for telecom wavelengths based on a PPLN waveguide," Opt. Express **24**, 23992–24001 (2016).
9. L. Chang, Y. Li, N. Volet, L. Wang, J. Peters, and J. E. Bowers, "Thin film wavelength converters for photonic integrated circuits," Optica **3**, 531–535 (2016).
10. A. Rao, M. Malinowski, A. Honardoost, J. R. Talukder, P. Rabiei, P. Delfyett, and S. Fathpour, "Second-harmonic generation in periodically-poled thin film lithium niobate wafer-bonded on silicon," Opt. Express **24**, 29941–29947 (2016).
11. C. Wang, C. Langrock, A. Marandi, M. Jankowski, M. Zhang, B. Desiatov, M. M. Fejer, and M. Lončar, "Ultrahigh-efficiency wavelength conversion in nanophotonic periodically poled lithium niobate waveguides," Optica **5**, 1438–1441 (2018).
12. J.-Y. Chen, Y. M. Sua, Z.-H. Ma, C. Tang, Z. Li, and Y.-P. Huang, "Efficient parametric frequency conversion in lithium niobate nanophotonic chips," OSA Continuum **2**, 2914–2924 (2019).
13. A. Boes, L. Chang, M. Knoerzer, T. G. Nguyen, J. D. Peters, J. E. Bowers, and A. Mitchell, "Improved second harmonic performance in periodically poled LNOI waveguides through engineering of lateral leakage," Opt. Express **27**, 23919–23928 (2019).
14. A. Rao, K. Abdelsalam, T. Sjaardema, A. Honardoost, G. F. Camacho-Gonzalez, and S. Fathpour, "Actively-monitored periodic-poling in thin-film lithium niobate photonic waveguides with ultrahigh nonlinear conversion efficiency of $4600\%W^{-1}cm^{-2}$," Opt. Express **27**, 25920–25930 (2019).
15. K. R. Parameswaran, R. K. Route, J. R. Kurz, R. V. Roussev, M. M. Fejer, and M. Fujimura, "Highly efficient second-harmonic generation in buried waveguides formed by annealed and reverse proton exchange in periodically poled lithium niobate," Opt. Lett. **27**, 179–181 (2002).
16. J. Lu, J. B. Surya, X. Liu, A. W. Bruch, Z. Gong, Y. Xu, and H. X. Tang, "Periodically poled thin film lithium niobate microring resonators with a second-harmonic generation efficiency of 250,000%/W," Optica **6**, 1455–1460 (2019).
17. M. Rüsing, C. Eigner, P. MacKwitz, G. Berth, C. Silberhorn, and A. Zrenner, "Identification of ferroelectric domain structure sensitive phonon modes in potassium titanyl phosphate: A fundamental study," J. Appl. Phys. **119**, 044103 (2016).
18. M. Rüsing, S. Neufeld, J. Brockmeier, C. Eigner, P. Mackwitz, K. Spychala, C. Silberhorn, W. G. Schmidt, G. Berth, A. Zrenner, and S. Sanna, "Imaging of 180 ferroelectric domain walls in uniaxial ferroelectrics by confocal Raman spectroscopy: Unraveling the contrast mechanism," Phys. Rev. Mater. **2**, 103801 (2018).
19. V. Y. Shur and P. S. Zelenovskiy, "Micro- and nanodomain imaging in uniaxial ferroelectrics: Joint application of optical, confocal Raman, and piezoelectric force microscopy," J. Appl. Phys. **116**, 066802 (2014).
20. S. I. Bozhevolnyi, J. M. Hvam, K. Pedersen, F. Laurell, H. Karlsson, T. Skettrup, and M. Belmonte, "Second-harmonic imaging of ferroelectric domain walls," Appl. Phys. Lett. **73**, 1814–1816 (1998).
21. S. Kurimura and Y. Uesu, "Application of the second harmonic generation microscope to nondestructive observation of periodically poled ferroelectric domains in quasi-phase-matched wavelength converters," J. Appl. Phys. **81**, 369–375 (1997).
22. M. Flörsheimer, R. Paschotta, U. Kubitscheck, C. Brillert, D. Hofmann, L. Heuer, G. Schreiber, C. Verbeek, W. Sohler, and H. Fuchs, "Second-harmonic imaging of ferroelectric domains in $LiNbO_3$ with micron resolution in lateral and axial directions," Appl. Phys. B **67**, 593–599 (1998).
23. P. Mackwitz, M. Rüsing, G. Berth, A. Widhalm, K. Müller, and A. Zrenner, "Periodic domain inversion in x-cut single-crystal lithium niobate thin film," Appl. Phys. Lett. **108**, 152902 (2016).
24. G. Berth, V. Quiring, W. Sohler, and A. Zrenner, "Depth-resolved analysis of ferroelectric domain structures in Ti:PPLN waveguides by nonlinear confocal laser scanning microscopy," Ferroelectrics **352**, 78–85 (2007).
25. S. Cherifi-Hertel, H. Bulou, R. Hertel, G. Taupier, K. D. H. Dorkenoo, C. Andreas, J. Guyonnet, I. Gaponenko, K. Gallo, and P. Paruch, "Non-Ising and chiral ferroelectric domain walls revealed by nonlinear optical microscopy," Nat. Commun. **8**, 15768 (2017).
26. J. Kaneshiro, Y. Uesu, and T. Fukui, "Visibility of inverted domain structures using the second harmonic generation

microscope: Comparison of interference and non-interference cases," J. Opt. Soc. Am. B **27**, 888–894 (2010).
27. J. Zhao, M. Rüsing, M. Roeper, L. M. Eng, and S. Mookherjea, "Poling thin-film x-cut lithium niobate for quasi-phase matching with sub-micrometer periodicity," J. Appl. Phys. **127**, 193104 (2020).
28. M. Rüsing, J. Zhao, and S. Mookherjea, "Second harmonic microscopy of poled x-cut thin film lithium niobate: Understanding the contrast mechanism," J. Appl. Phys. **126**, 114105 (2019).
29. L. He, M. Zhang, A. Shams-Ansari, R. Zhu, C. Wang, and M. Loncar, "Low-loss fiber-to-chip interface for lithium niobate photonic integrated circuits," Opt. Lett. **44**, 2314–2317 (2019).
30. D. A. Stocker, E. F. Schubert, W. Grieshaber, K. S. Boutros, and J. M. Redwing, "Facet roughness analysis for InGaN/GaN lasers with cleaved facets," Appl. Phys. Lett. **73**, 1925–1927 (1998).
31. T. Umeki, O. Tadanaga, and M. Asobe, "Highly efficient wavelength converter using direct-bonded PPZnLN ridge waveguide," IEEE J. Quantum Electron. **46**, 1206–1213 (2010).
32. M. Chauvet, F. Henrot, F. Bassignot, F. Devaux, L. Gauthier-Manuel, V. Pecheur, H. Maillotte, and B. Dahmani, "High efficiency frequency doubling in fully diced $LiNbO_3$ ridge waveguides on silicon," J. Opt. **18**, 085503 (2016).
33. M. Neradovskiy, E. Neradovskaia, D. Chezganov, E. Vlasov, V. Y. Shur, H. Tronche, F. Doutre, G. Ayenew, P. Baldi, M. De Micheli, and C. Montes, "Second harmonic generation in periodically poled lithium niobate waveguides with stitching errors," J. Opt. Soc. Am. B **35**, 331–336 (2018).
34. L. Gui, "Periodically Poled Ridge Waveguides and Photonic Wires in $LiNbO_3$ for Efficient Nonlinear Interactions," Ph.D. thesis, University of Paderborn (2010).
35. O. Gayer, Z. Sacks, E. Galun, and A. Arie, "Temperature and wavelength dependent refractive index equations for MgO-doped congruent and stoichiometric $LiNbO_3$," Appl. Phys. B **91**, 343–348 (2008).
36. I. H. Malitson, "Interspecimen Comparison of the Refractive Index of Fused Silica*†," J. Opt. Soc. Am. **55**, 1205–1209 (1965).
37. J. H. Wray and J. T. Neu, "Refractive Index of Several Glasses as a Function of Wavelength and Temperature*," J. Opt. Soc. Am. **59**, 774–776 (1969).
38. R. L. Sutherland, *Handbook of Nonlinear Optics* (Marcel Dekker, 2003).
39. P. Weigel and S. Mookherjea, "Design of folded hybrid silicon carbide-lithium niobate waveguides for efficient second-harmonic generation," J. Opt. Soc. Am. B **35**, 593–600 (2018).